NeuroImage: Clinical 42 (2024) 103593

Contents lists available at ScienceDirect

NeuroImage: Clinical

journal homepage: www.elsevier.com/locate/ynicl

Comparative overview of multi-shell diffusion MRI models to characterize the microstructure of multiple sclerosis lesions and periplaques

Colin Vanden Bulcke [a,b,*], Anna Stölting [a], Dragan Maric [c], Benoît Macq [b], Martina Absinta [d], Pietro Maggi [a,e,*]

[a] Neuroinflammation Imaging Lab (NIL), Institute of NeuroScience, Université catholique de Louvain, Brussels, Belgium
[b] ICTEAM Institute, Université catholique de Louvain, Louvain-la-Neuve, Belgium
[c] Flow and Imaging Core Facility, National Institute of Neurological Disorders and Stroke, National Institutes of Health, Bethesda, MD, USA
[d] Translational Neuropathology Unit, Institute of Experimental Neurology, Division of Neuroscience, IRCCS San Raffaele Scientific Institute, Milan, Italy
[e] Department of Neurology, Cliniques universitaires Saint-Luc, Université catholique de Louvain, Brussels, Belgium

ARTICLE INFO

Keywords:
Multiple Sclerosis
MRI
Diffusion microstructural modelling
Neuroinflammation
Histopathology

ABSTRACT

In multiple sclerosis (MS), accurate *in vivo* characterization of the heterogeneous lesional and extra-lesional tissue pathology remains challenging. Marshalling several advanced imaging techniques — quantitative relaxation time (T1) mapping, a model-free average diffusion signal approach and four multi-shell diffusion models — this study investigates the performance of multi-shell diffusion models and characterizes the microstructural damage within (i) different MS lesion types — active, chronic active, and chronic inactive — (ii) their respective periplaque white matter (WM), and (iii) the surrounding normal-appearing white matter (NAWM). In 83 MS participants (56 relapsing-remitting, 27 progressive) and 23 age and sex-matched healthy controls (HC), we analysed a total of 317 paramagnetic rim lesions (PRL+), 232 non-paramagnetic rim lesions (PRL-), 38 contrast-enhancing lesions (CEL). Consistent with previous findings and histology, our analysis revealed the ability of advanced multi-shell diffusion models to characterize the unique microstructural patterns of CEL, and to elucidate their possible evolution into a resolving (chronic inactive) vs smoldering (chronic active) inflammatory stage. In addition, we showed that the microstructural damage extends well beyond the MRI-visible lesion edge, gradually fading out while moving outward from the lesion edge into the immediate WM periplaque and the NAWM, the latter still characterized by diffuse microstructural damage in MS vs HC. This study also emphasizes the critical role of selecting appropriate diffusion models to elucidate the complex pathological architecture of MS lesions and their periplaque. More specifically, multi-compartment diffusion models based on biophysically interpretable metrics such as neurite orientation dispersion and density (NODDI; mean auc=0.8002) emerge as the preferred choice for MS applications, while simpler models based on a representation of the diffusion signal, like diffusion tensor imaging (DTI; mean auc=0.6942), consistently underperformed, also when compared to T1 mapping (mean auc=0.73375).

1. Introduction

Multiple Sclerosis (MS) is the most prevalent chronic inflammatory-mediated disease of the central nervous system (CNS), mostly characterized by recurring neurological symptoms and associated with focal demyelinated lesions in the brain and spinal cord (Reich et al., 2018). Up to this time, microstructural investigation of MS-associated brain tissue damage remains challenging, primarily because of the lack of accurate methods able to depict the heterogeneous nature of MS pathology *in vivo*. MS lesions are indeed heterogeneous in terms of inflammatory response, myelin and axonal damage (Lucchinetti et al., 2000). In their initial stage, they are usually characterized by opening of the blood–brain barrier, causing perivascular and parenchymal acute inflammation (Reich et al., 2018). During this acute-early phase, lesions typically appear as contrast-enhancing on gadolinium-based magnetic resonance imaging (MRI) (Campbell et al., 2012). Once this initial phase of acute inflammation resolves (lasting about 4–8 weeks), newly formed lesions can either evolve into a chronic inactive stage, associated with variable

* Corresponding authors.
E-mail addresses: colin.vandenbulcke@uclouvain.be (C. Vanden Bulcke), pietro.maggi@uclouvain.be (P. Maggi).

https://doi.org/10.1016/j.nicl.2024.103593
Received 12 December 2023; Received in revised form 1 March 2024; Accepted 16 March 2024
Available online 18 March 2024

degrees of remyelination, or into a chronic active stage, which is characterized by a continuous smoldering inflammatory process at the lesion edge. Indeed, as seen on *ex vivo* histopathology, chronic active lesions feature an inactivated core and a peripheral rim of activated microglia/macrophages containing paramagnetic iron and are detectable on susceptibility-based MRI as paramagnetic rim lesions (PRL) (Absinta et al., 2016; Maggi et al., 2020). These lesions are characterized by extensive tissue damage and are associated with increased levels of neuro-filament light chain in the peripheral blood (Maggi et al., 2021) as well as with lower brain volumes (Absinta et al., 2019; Hemond et al., 2022). From a clinical point of view, chronic active lesions are correlated with disease severity and progression (Absinta et al., 2019; Maggi et al., 2020, 2023). Beyond focal tissue damage, advanced MRI techniques can also depict *in vivo* diffuse pathological changes in the normal-appearing white matter (NAWM) of MS patients (Kutzelnigg et al., 2005). *Ex vivo* histopathological studies suggest that these extra-lesional pathological changes are even more pronounced in the immediate periplaque of MS lesions (Dal-Bianco et al., 2021). At present, only few studies have investigated *in vivo* the microstructural damage of the MS lesions periplaque (Hu et al., 2022; Krajnc et al., 2023; Rahmanzadeh et al., 2021) and, to our knowledge, comparative analyses of active, chronic active and chronic inactive MS lesions periplaques are lacking.

MRI offers invaluable insight into the neuropathological aspects of multiple sclerosis within living patients. Quantitative longitudinal relaxation (T1) time has been widely used in the past to describe MS lesions, given its high correlation with myelination and axonal density in MS (Kolb et al., 2021). Additionally, multi-shell diffusion MRI stands out as a widely used method to quantify *in vivo* the microstructure of MS tissue, showing enhanced pathological specificity and correlation to clinical outcomes (Hori et al., 2022; Mustafi et al., 2019; Rahmanzadeh et al., 2021). However, various diffusion models have been implemented, each with unique intrinsic characteristics derived from assumptions and specific optimization processes. This results in distinctive metrics which reflect the diffusion of water molecules and/or biophysically interpretable brain compartments, exhibiting varying degrees of correlation with *in vivo* biology (Novikov et al., 2018). This study employs four different diffusion models to characterize the microstructural damage patterns in different MS lesion types, in their periplaque and in the surrounding NAWM. Moreover, we conduct a comparative analysis of these diffusion models, relative to a model-free diffusion signal representation, revealing their strengths and weaknesses in the context of MS.

2. Materials and methods

2.1. Participants

Imaging and clinical data were consecutively collected under an institutional review board-approved protocol in adults with a diagnosis of MS followed at Cliniques Universitaires Saint-Luc (CUSL). Specific patient inclusion criteria were the following: (1) age $\geq$18 years, (2) diagnosis of MS based on the 2017 McDonald criteria (Thompson et al., 2018), and (3) availability of 3-Tesla (3T) 3-dimensional (3D) post-contrast T1-weighted image (for active lesion assessment), T2*-weighted echo-planar imaging (EPI) (Sati et al., 2014) (for chronic active lesion assessment), T2-weighted fluid-attenuated inversion recovery (FLAIR) (for lesion segmentation), T1-weighted magnetization prepared rapid gradient echo image (MPRAGE) (for automatic NAWM assessment), quantitative T1-map derived from a sagittal 3D magnetization-prepared 2 rapid gradient echo (MP2RAGE) and multi-shell diffusion-weighted images (for microstructural investigations). Imaging data of adults presenting no clinical/MRI evidence of CNS disease, hereafter healthy controls (HC), were also additionally collected. Overall, a total of 83 MS participants (56 relapsing-remitting — RRMS —, 18 secondary-progressive — SPMS — and 9 primary-progressive — PPMS) and 23 age and gender-matched healthy controls (HC) were included in the study. This study was approved by the local ethical committee of CUSL and all participants provided written informed consent prior to the study.

2.2. Human neuropathology

Seven formalin-fixed paraffin-embedded brain tissue samples from 7 progressive MS (PMS) autopsy cases (5 women, average age 50 years old, age range 43–61 years), including lesions at different pathological stages (active, chronic active and chronic inactive lesions), were provided by the Netherlands Brain Bank. Neuropathological analysis included multiplex immunofluorescence (Absinta et al., 2021) and evaluation of myelin basic protein (MBP) — a marker for myelin and oligodendrocytes —, neurofilament heavy chain (NFH) — a marker for axonal integrity — and of human leukocyte antigen - DR isotope (HLADR) — a marker for myeloid antigen-presenting cells. Using ImageJ/Fiji software, we performed a semi-quantitative immunostaining analysis based on the z-score normalization of specific area compared to the whole tissue. The post-mortem human brain tissue samples were used as an illustrative aid to better interpret the diffusion MRI results.

2.3. MRI imaging protocol

MRI acquisition was performed on a 3T whole-body MR scanner (GE SIGNA^{TM} Premier research scanner, General Electric, Milwaukee, WI) equipped with a 48-channel head coil. The MRI protocol for MS participants included: (i) sagittal 3D MPRAGE sequence (repetition time (TR)=2186 ms, echo-time (TE)=3 ms, inversion time (TI)=900 ms, field of view (FOV)=256 mm, number of slices (#slices)=156, voxel size=1.0x1.0x1.0 mm), (ii) sagittal 3D FLAIR sequence (TR=5000 ms, TE=105 ms, TI=1532 ms, FOV=256 mm, #slices=170, voxel size=1.0x1.0x1.0 mm), (iii) a sagittal high-resolution 3D EPI (Sati et al., 2014) sequence (TR=80.2 ms, TE=35 ms, flip angle=18°, FOV=256 mm, #slices=355, voxel size=0.67x0.67x0.67 mm), (iv) quantitative T1-map derived from a sagittal 3D MP2RAGE sequence (TR=1925 ms, TE=3 ms, TI=700 and 2500 ms, FOV=256 mm, #slices=156, voxel size=1.0x1.0x1.0 mm), (v) multi-shell diffusion-weighted sequence (TR=4842 ms, TE=77 ms, Δ=35.7 ms, δ=22.9 ms, 64 gradients at b=1000, 32 at b=2000,3000,5000 and 7b=0 s/mm^2, FOV=220, #slices=68, voxel size=2.0x2.0x2.0) with reversed phase encoding, and (vi) a post-gadolinium T1-weighted spoiled gradient recalled echo (CE-SPGR) sequence (TR=6.9 ms, TE=2.1 ms, flip angle=12°, FOV=240, #slices=150, voxel size=0.69x0.69x1.0 mm). MRI protocol for HC only included the same MPRAGE and multi-shell diffusion-weighted sequence.

2.4. Region of interest identification and segmentation

We investigated the following WM regions of interest (ROI): (i) acute contrast-enhancing lesions (CEL) and non-enhancing lesions bearing or not a paramagnetic rim (respectively, PRL+ and PRL-), (ii) the periplaque of the above-mentioned lesions (respectively, *peri*-CEL, *peri*-PRL+, *peri*-PRL-), and (iii) the NAWM of MS participants and HC (respectively, NAWM-MS and NAWM-HC). To this end, 3D FLAIR and post-gadolinium CE-SPGR images were rigidly coregistered to the high-resolution 3D EPI scan using ANTs (Avants et al., 2008). CEL were identified as lesions showing contrast enhancement on the post-gadolinium CE-SPGR image. Besides, a chronic non-enhancing MS lesion was defined as a PRL+ if it exhibited no enhancement on the post-gadolinium CE-SPGR image and a paramagnetic rim on unwrapped-filtered phase images (Absinta et al., 2013) according to the latest consensus statement (Bagnato et al., 2024) with the following features as previously described (Maggi et al., 2023): (i) colocalization with the edge of an MS lesion on FLAIR image, (ii) visibility on at least two planes, and (iii) paramagnetic rim covering at least 2/3 of the lesion WM

edge on the slice of maximum visibility. PRL assessment was determined by consensus of 2 trained raters (AS and PM), and manually segmented on the coregistered FLAIR image by AS using ITK-SNAP (https://www.itksnap.org). PRL- was defined as chronic non-enhancing lesions showing no visible paramagnetic rim on unwrapped-filtered phase images. Lesions with a volume smaller than 24 mm^3 (corresponding to a minimum of three voxels in the diffusion resolution) and paramagnetic rim lesions not fulfilling the PRL+ criteria (Bagnato et al., 2024) were excluded from the analysis. Overall, 587 lesions (317 PRL+, 232 PRL-, and 38 CEL) were included in the analysis. NAWM mask was automatically computed based on FreeSurfer brain segmentation (Fischl et al., 2002) and corrected by subtracting a lesion mask segmented using SAMSEG software (Cerri et al., 2021) and a ventricle mask computed using an in-house algorithm based on Otsu thresholding (Otsu, 1979). The segmentation of the periplaque was automatically computed by expanding the lesion boundary by 3 mm into the surrounding NAWM using an in-house algorithm. NAWM areas surrounding more than one lesion type were excluded from the periplaque analysis. Periplaque segmentations were then subtracted from the NAWM segmentation mask for the final analysis. An illustration of every ROI and their segmentation is displayed in Fig. 1. Data management, registration and segmentation were managed using the BIDS Managing and Analysis Tool (Vanden Bulcke et al., 2022).

2.5. Microstructural investigations

Microstructural tissue integrity was investigated using two quantitative imaging methods: quantitative longitudinal relaxation time (T1) derived from the MP2RAGE sequence (MP2RAGE-derived T1map) — used as an established marker of MS tissue integrity (Kolb et al., 2021) — and multi-shell diffusion MRI, in order to further investigate microstructural alterations. The multi-shell diffusion data were first preprocessed with denoising (Veraart et al., 2016), top-up (Andersson et al., 2003), motion and eddy-currents correction (Andersson & Sotiropoulos, 2016), and skull-stripping using FSL BET (Jenkinson et al., 2005). It was then processed in one model-free approach and by four different diffusion models of WM detailed hereunder:

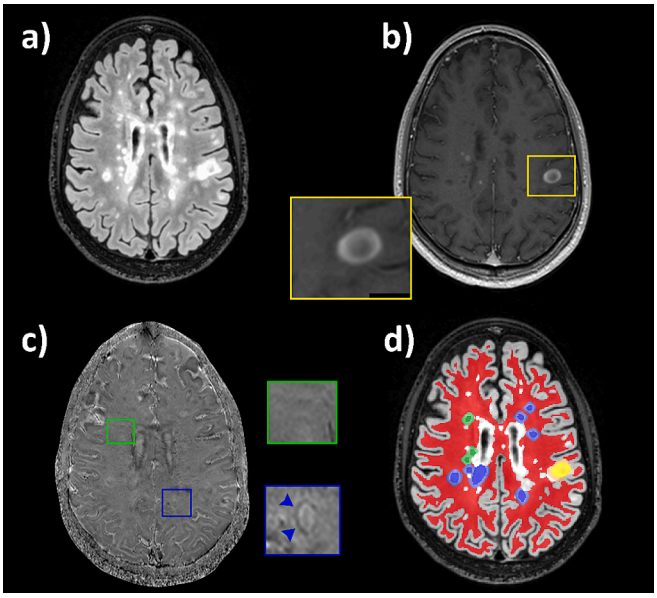

Fig. 1. (a, d) Axial FLAIR image of a 25-year-old man with RRMS showing different types of white-matter lesions, their periplaque and the normal-appearing white matter (NAWM). (b) A typical contrast-enhancing lesion (CEL — yellow box) is visible on the post-gadolinium CE-SPGR. (c) Chronic non-enhancing paramagnetic rim lesions (PRL+) and non-paramagnetic rim lesions (PRL-) can be observed on the axial filtered unwrapped-phase image (respectively blue and green boxes). In (d), the NAWM is segmented in red while CEL, PRL+, and PRL- are respectively segmented in yellow, blue, and green; lesions' periplaques are segmented and displayed using similar desaturated colors.

- The model-free approach consists of computing the average diffusion signal on each shell. This approach was employed to inspect the sensitivity differences between multi-shell and single-shell diffusion schemes, as well as the sensitivity of each *b*-value within the scheme for characterizing MS lesion pathology.
- Diffusion Tensor Imaging (DTI) (Alexander et al., 2007) is a robust single-compartment and widely used diffusion model that characterizes the diffusivity of water molecules within tissue as a single fiber population per voxel. DTI was computed using the multi-shell diffusion scheme with a weighted linear least squares estimation of the diffusion parameters (Veraart et al., 2013). This model was used to study axial diffusivity (AD_{DTI}), radial diffusivity (RD_{DTI}), mean diffusivity (MD_{DTI}), and fractional anisotropy (FA_{DTI}) which are correlated to axonal integrity, myelination, fiber integrity, and tissue integrity respectively. However, DTI suffers from low biological interpretability of its diffusion metrics, as they are influenced by multiple microstructural features.
- DIstribution of Anisotropic MicrOstructural eNvironments in DWI (DIAMOND) (Scherrer et al., 2016) model is a diffusion model capable of describing multiple crossing fiber populations. DIAMOND metrics correspond to a fiber population-weighted version of the DTI metrics (AD_{DMD}, RD_{DMD}, MD_{DMD} and FA_{DMD}) with a supplementary free water compartment ($fcsf_{DMD}$). Therefore, DIAMOND overcomes some limitations of DTI but somehow suffers from the same lack of metrics interpretability.
- Neurite Orientation Dispersion and Density Imaging (NODDI) (Zhang et al., 2012) is a multi-compartment model aiming at characterizing neurite orientation dispersion. Contrarily to DTI, NODDI computes a set of biologically interpretable metrics as the fraction of intra-axonal volume (icvf), the fraction of extra-axonal cell volume (ecvf), the fraction of isotropic diffusivity (fiso), and the orientation dispersion index of the fibers (odi). NODDI's limitations come from its two assumptions: (i) one fiber population per voxel and (ii) fixed diffusivity for all the voxels in the brain tissue.
- Different from the three previously described models which are analytical diffusion models, making assumptions about the tissue's diffusion processes often digressing from the biophysical reality, Microstructure Fingerprinting (MF) (Rensonnet et al., 2019) is a novel numerical diffusion model that uses pre-computed Monte Carlo simulations of water molecules random-walk in complex 3D configurations representative of WM tissue, in order to estimate biophysically interpretable microstructural parameters. MF was designed to be specific to the fiber volume fraction (fvf) correlated to axonal volume fraction, and the fraction of free water ($fcsf_{MF}$).

2.6. Statistical analysis

Statistical analysis was performed using R and Jamovi (https://www.jamovi.org). Age comparisons between MS participants and HC as well as between RRMS and PMS participants were performed by independent samples t-tests, and Fischer's exact test was used for gender comparisons. Non-parametric Mann-Whitney *U* test was used to compare lesions population between RRMS and PMS participants. The different methods used for the microstructural tissue investigation were compared for area under the curve (auc), accuracy, sensitivity and specificity using a support vector machine (SVM) classifier through the computation of a receiver operating characteristic (ROC) curve. When evaluated on multiple differentiating tasks, the mean auc and the variance of auc — as a proxy of the model's stability across several differentiation tasks — were used to compare the different models between one another. Finally, Whelch's ANOVA and Games-Howell *post-hoc* tests

were used to compare the MRI metrics among the different investigated ROI and p-values <0.05, <0.01, <0.001, were considered significant (*), very significant (**), and strongly significant (***) respectively.

3. Results

3.1. MS phenotype comparison

Table 1 summarizes the MS cohort characteristics. The MS cohort was composed of 56 participants diagnosed with an RRMS phenotype and 27 with a PMS phenotype (18 SPMS, 9 PPMS). PMS participants were older ($p<0.001$) and had longer disease duration ($p<0.001$) than RRMS participants, but no statistical difference in sex distribution was found between the two groups. Compared to RRMS, no PMS participants born any CEL, and no statistical differences were found in terms of number and total volume load of PRL+ and PRL- between the two MS phenotypes.

A complete comparison of the microstructural metrics of PRL+ and PRL- core between the RRMS and PMS participants is described in the supplementary materials (Table S1). In summary, when compared to PRL+ in RRMS, PRL+ in PMS participants were bigger ($p<0.01$) and had longer T1 ($p<0.001$), suggesting more tissue damage. On the contrary, PRL- in PMS participants were characterized by lower MD_{DMD} ($p<0.01$), RD_{DMD} ($p<0.01$) and ecvf ($p<0.01$), potentially reflecting time-dependent recovery/repair in chronic inactive MS lesions.

3.2. Multi-shell vs. single-shell model-free analysis

Fig. 2 presents an axial view of average diffusion-weighted MRI images acquired with different *b*-values. From visual inspection, we can observe that higher *b*-values (typically b=5000 s/mm^2) are more sensitive to compartments with high restrained diffusivity such as those found in the white matter microstructure (e.g. axon bundle). However, higher *b*-values are also more sensitive to noise. In addition, certain lesions are nearly invisible at certain *b*-values (b=2000 or b=3000 s/mm^2).

As a more quantitative analysis, the performance of each shell to differentiate between PRL+ and PRL- lesions is reported in Table 2. Multi-shell acquisition scheme showed the best performance (auc=0.7292) to differentiate between PRL+ and PRL- lesions. When using only one shell, *b*-value=5000 s/mm^2 showed the best performance (auc=0.6943), followed by *b*-value=1000 s/mm^2 (auc=0.6842), *b*-value=0 s/mm^2 (auc=0.6826), *b*-value=3000 s/mm^2 (auc=0.6497), and *b*-value=2000 s/mm^2 (auc=0.6171).

Table 1
Multiple Sclerosis cohort characteristics.

	RRMS	PMS (SPMS, PPMS)	Statistical analysis
Participants, n	56	27 (18, 9)	n/a
Women, n (%)	39 (69.64 %)	15 (55.56 %)	p=0.207
Age, mean (range) [years]	39.5 (19.3–67.3)	52.8 (32.7–72.0)	**p<0.001**
Disease duration, mean ±std [years]	5.46±6.63	14.9±10.8	**p<0.001**
PRL+, n (mean±std)	239 (4.27 ±11.54)	78 (2.89±3.99)	p=0.8382
PRL-, n (mean±std)	157 (2.8 ±3.98)	75 (2.78±4.07)	p=0.7929
CEL, n (mean±std)	38 (0.68 ±1.65)	0	n/a
PRL+, volume load (mean ±std) [mm^3]	696±1931.15	845.4±1539.65	p=0.8109
PRL-, volume load (mean ±std) [mm^3]	204.34 ±335.42	306.27±611.51	p=0.583
CEL, volume load (mean ±std) [mm^3]	192.9±563.96	n/a	n/a

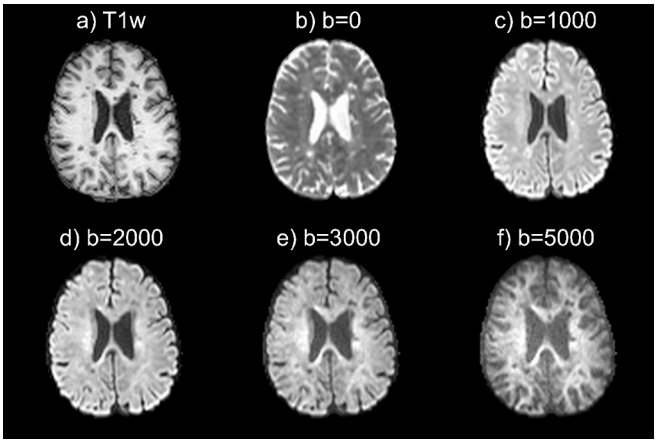

Fig. 2. Axial T1- (a) and average diffusion-weighted MRI (b-f) images of a 28-year-old woman with RRMS showing the influence of *b*-value in the sensitivity for specific brain tissue. Higher *b*-values (b=3000, b=5000 s/mm^2) are more sensitive to white matter and white matter alteration (i.e. lesions), but noisier compared to lower *b*-values (b=1000 s/mm^2).

3.3. Comparison of the different diffusion models

The relative performance of each diffusion model to differentiate between the different types of lesions, and their WM periplaque is reported in Table 3. Overall (i.e., across all analyzed lesional and periplaque ROI) NODDI showed the best performance (mean auc=0.8002) followed by MF (mean auc=0.7488), DIAMOND (mean auc=0.7445), T1 (mean auc=0.73375), and DTI (mean auc=0.6942). Besides, DIAMOND appeared to be the most stable model (variance=0.000239) followed by MF (variance=0.001160), NODDI (variance=0.001764), T1 (variance=0.002605) and DTI (variance=0.003188). Finally, the mean rank of each model across all applications is 1.16 for NODDI, 2.83 for DIAMOND, 3 for MF, 3.83 for T1 and 4.16 for DTI.

3.4. MRI analysis of MS lesions' microstructural damage

The main results of the lesions' in-vivo MRI microstructure characterization are reported in Fig. 3. Additional diffusion models' parameters and statistical analysis results are reported in Figure S1 and Table S2 of the supplementary materials.

3.4.1. Lesions

When compared to PRL-, PRL+ were characterized by a more pronounced tissue damage. Specifically, PRL+ were characterized by an overall decreased tissue integrity with longer T1 ($p<0.001$), higher MD_{DTI} and MD_{DMD} ($p<0.001$), and lower FA_{DTI} and FA_{DMD} ($p<0.001$), by increased axonal damage with lower icvf and fvf ($p<0.001$), by more demyelination with higher RD_{DTI} and RD_{DMD} ($p<0.001$), and by more pronounced cellular infiltration with higher ecvf ($p<0.001$). CEL lesions, with respect to PRL-, showed similar values of MD_{DTI} (vs. PRL-: $p=0.913$; vs. PRL+: $p<0.01$) and icvf (vs. PRL-: $p=0.998$; vs. PRL+: $p<0.05$), whereas they resembled PRL+ in terms of RD_{DMD} (vs. PRL-: $p<0.05$; vs. PRL+: $p=1$), fvf (vs. PRL-: $p<0.01$; vs. PRL+: $p=1$), ecvf (vs. PRL-: $p<0.05$; vs. PRL+: $p=0.315$), FA_{DTI} (vs. PRL-: $p<0.001$; vs. PRL+: $p=0.262$) and FA_{DMD} (vs. PRL-: $p<0.001$; vs. PRL+: $p=0.219$). CEL showed T1 relaxation times in between PRL- ($p<0.05$) and PRL+ ($p<0.05$) and pronounced edema with a tendency towards higher $fcsf_{MF}$ values when compared to PRL- ($p=0.078$).

3.4.2. Lesions' periplaque

The comparison between the periplaque of PRL+ and PRL- yielded similar, although more subtle results, to the ones obtained for the lesion parenchyma. Indeed, compared to *peri*-PRL-, *peri*-PRL+ were

Table 2
Receiver operating characteristic (ROC) curve analysis comparing the ability of the average diffusion signal computed on different shells (b=0, 1000, 2000, 3000, 5000 s/mm^2) and the whole multi-shell scheme to differentiate between chronic active (PRL+) and chronic inactive (PRL-) lesions. The table displays a summary of the full performance (area under the curve (auc), accuracy, sensitivity, specificity) from the ROC curve analysis.

	b=0	b=1000	b=2000	b=3000	b=5000	Multi-shell
auc	0,6826	0,6842	0,6171	0,6497	0,6943	**0,7292**
accuracy	0,6007	0,6259	0,5737	0,5773	0,6421	**0,6457**
sensitivity	0,4489	0,582	0,4644	0,4768	**0,7059**	0,5666
specificity	**0,8112**	0,6867	0,7253	0,7167	0,5536	0,7554

Table 3
Receiver operating characteristic (ROC) curve analysis comparing the ability of the different diffusions models and quantitative T1map to differentiate between different regions of interest (ROI). The table displays a summary of the full performance (auc, accuracy, sensitivity, specificity) of each model for differentiating ROI between one another and their mean performance across all applications. Abbreviations: area under the curve (auc); periplaque of paramagnetic rim lesion (pPRL+); periplaque of non-paramagnetic rim lesion (pPRL-); periplaque of contrast enhancing lesion (pCEL); Diffusion Tensor Imaging (DTI); DIstribution of Anisotropic MicrOstructural eNvironments in DWI (DIAMOND); Neurite Orientation Dispersion and Density Imaging (NODDI); Microstructure Fingerprinting (MF); Quantitative longitudinal relaxation time (T1).

		PRL+~PRL-	pPRL+~pPRL-	PRL+~CEL	pPRL+~pCEL	CEL ~ PRL-	pCEL ~ pPRL-	mean	variance
DTI	auc	0,6922	0,6152	0,735	0,7095	0,7785	0,6349	0,6942	0,003188
	accuracy	0,6284	0,6029	0,6141	0,6275	0,7259	0,7168	0,6526	–
	sensitivity	0,5268	0,3576	0,6025	0,6203	0,7368	0,4878	0,5996	–
	specificity	0,7672	0,9286	0,7105	0,6829	0,7241	0,7563	0,7616	–
DIAMOND	auc	0,7302	0,7265	0,7507	0,7329	0,7608	0,7661	0,7445	**0,000239**
	accuracy	0,652	0,6352	0,6875	0,5892	0,7037	0,7986	0,6777	–
	sensitivity	0,5	0,4601	0,6879	0,5687	0,6316	0,575	0,5706	–
	specificity	0,8578	0,8655	0,6842	0,75	0,7155	0,8361	0,7849	–
NODDI	auc	0,8167	**0,765**	**0,8419**	**0,7369**	**0,8556**	**0,7852**	**0,8002**	0,001764
	accuracy	0,7468	0,6787	0,7859	0,6919	0,7963	0,681	0,7301	–
	sensitivity	0,7571	0,6139	0,795	0,6994	0,6842	0,8293	0,7298	–
	specificity	0,7328	0,7647	0,7105	0,6341	0,8147	0,6555	0,7187	–
MF	auc	0,7786	0,7126	0,7199	0,7141	0,7955	0,7721	0,7488	0,00116
	accuracy	0,6995	0,6047	0,6	0,6891	0,7778	0,7061	0,6795	–
	sensitivity	0,7161	0,4082	0,5868	0,6994	0,7368	0,5854	0,6221	–
	specificity	0,6767	0,8655	0,7105	0,6098	0,7845	0,7269	0,729	–
T1	auc	**0,8422**	0,7241	0,7018	0,694	0,7001	0,7403	0,73375	0,002605
	accuracy	0,7596	0,6552	0,6535	0,7423	0,7259	0,6918	0,7047	–
	sensitivity	0,7161	0,6013	0,6562	0,7785	0,5789	0,6341	0,6609	–
	specificity	0,819	0,7269	0,6316	0,4634	0,75	0,7017	0,6821	–

characterized by less tissue integrity with longer T1 ($p<0.001$), higher MD_{DTI} and MD_{DMD} ($p<0.001$), and lower FA_{DTI} ($p<0.05$) and FA_{DMD} ($p<0.001$), by increased axonal damage with lower icvf and fvf ($p<0.001$), by more demyelination with higher RD_{DTI} and RD_{DMD} ($p<0.001$), and by more cellular infiltrate with higher ecvf ($p<0.001$). The periplaque of CEL, resembled the *peri*-PRL+ in terms of ecvf (vs. *peri*-PRL-: $p<0.001$; vs. *peri*-PRL+: $p=1$) and fvf (vs. *peri*-PRL-: $p<0.05$; vs. *peri*-PRL+: $p=0.993$).

3.4.3. NAWM vs. periplaque

Compared to the NAWM of HC, the NAWM of MS subjects showed a slight decrease in overall tissue integrity with higher MD_{DTI} and MD_{DMD} ($p<0.05$), more demyelination with higher RD_{DTI} ($p<0.05$), and increased cellular infiltration with higher ecvf ($p<0.01$). When the NAWM-MS was compared to the periplaque of each type of lesions, the first was characterized by more tissue integrity with lower MD_{DTI} and MD_{DMD} ($p<0.001$) and lower T1 value than *peri*-PRL+ ($p<0.001$), by more axonal integrity with higher icvf ($p<0.001$) and higher fvf than *peri*-CEL ($p<0.01$) and *peri*-PRL+ ($p<0.001$), by more myelination with lower RD_{DTI} and RD_{DMD} (vs. *peri*-PRL-: $p<0.01$; vs. *peri*-CEL: $p<0.01$; vs. *peri*-PRL+: $p<0.001$), by less cellular infiltrate with lower ecvf ($p<0.001$), and by lower $fcsf_{MF}$ than *peri*-PRL- and *peri*-PRL+ ($p<0.001$). Finally, when compared with the core of all lesion types, the NAWM-MS was clearly characterized by an overall less pathological tissue microstructure according to all microstructural metrics ($p<0.001$).

3.4.4. Periplaque vs. lesions core

For all the different lesion types, the periplaque vs lesion core was characterized by an increase in tissue integrity with shorter T1, lower MD_{DTI} and MD_{DMD}, and higher FA_{DTI} and FA_{DMD}, by more axonal integrity with higher icvf and fvf, by increased myelination lower RD_{DTI} and RD_{DMD}, and by less cellular infiltrate with lower ecvf. Interistingly, *peri*-CEL and *peri*-PRL+ were not statistically different from the core of PRL- in terms of cellular infiltrate with somewhat similar proportion of ecvf ($p=0.499$ for *peri*-CEL vs. PRL-; $p=0.064$ for *peri*-PRL + vs. PRL-).

3.5. Histological illustration of MS lesions and periplaques' microstructural damage

In Fig. 4, representative histopathological examples of MS lesions at different stages are shown. Three main pathological features were evaluated: (1) myelin content (MBP immunostaining), (2) axonal density (NFH immunostaining) and (3) HLADR+ activated microglia/macrophage infiltrate in three distinct locations; within the lesion core/edge, close periplaque (1; 0-2 mm) and distal periplaque (2; 2-4 mm).

The active lesion (Fig. 4.a) shows accumulation of myeloid cells in the center of the lesion, extending in the close periplaque, as well as demyelination and minimal axonal degeneration inside the lesion, with very subtle axonal damage in the close periplaque.

The chronic active lesion (Fig. 4.b) shows a gradient of demyelination and axonal loss between the core of the lesion and the periplaque, with infiltration of activated myeloid cells mostly taking place at the edge of the lesion.

The chronic inactive lesion (Fig. 4.c) shows scarce infiltration of activated myeloid cells and a less evident gradient of axonal degeneration between the core of the lesion and the periplaque, with no apparent

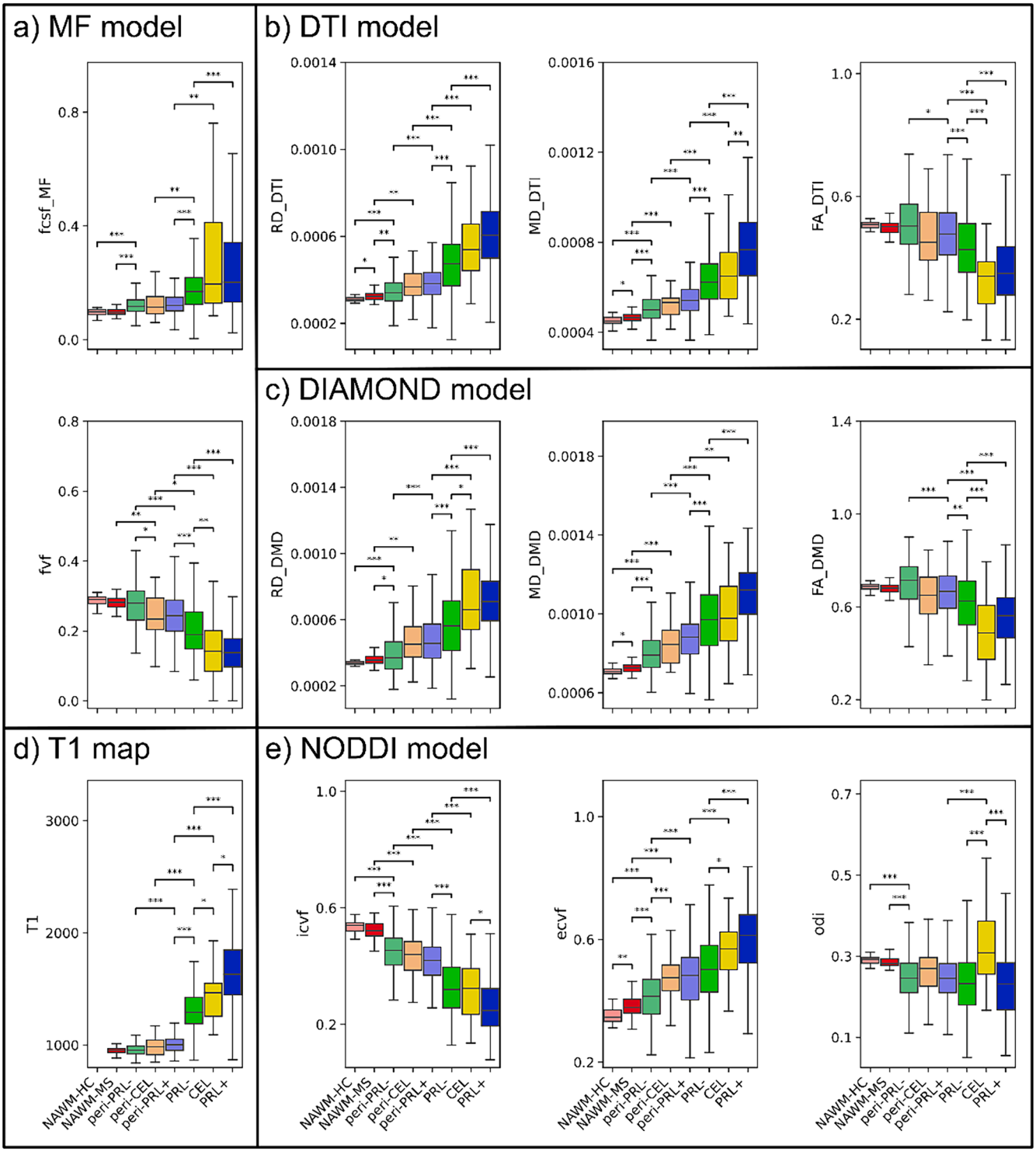

Fig. 3. Microstructure of different regions of interest (ROI) according to T1 (d) and 4 diffusion models; MF (a), DTI (b), DIAMOND (c), NODDI (e). On each graph, the different ROI are; NAWM-HC (desaturated red), NAWM-MS (red), *peri*-PRL- (desaturated green), *peri*-CEL (desaturated orange), *peri*-PRL+ (desaturated blue), PRL- (green), CEL (yellow), PRL+ (blue). The ROI are ordered by order of microstructural damage according to histopathological analysis. Statistical differences are only noted between ROI with a range of 2, with * ($p<0.05$), ** ($p<0.01$), *** ($p<0.001$).

demyelination in the periplaque.

4. Discussion

In this study, we employed one model-free approach and five distinct quantitative imaging techniques, including MP2RAGE-derived T1map and four diffusion models (DTI, DIAMOND, NODDI and MF), to investigate the microstructure of the principal types of MS WM lesions and their corresponding periplaque. In our cohort, PRL+ lesion core exhibited higher tissue damage in PMS participants when compared to RRMS participants, suggesting a continuous process of progressive tissue damage associated with longer disease duration (in PMS vs. RRMS). Interestingly, a less pathologic PRL- core in PMS participants could imply a potential time-dependent process of tissue repair in inactive

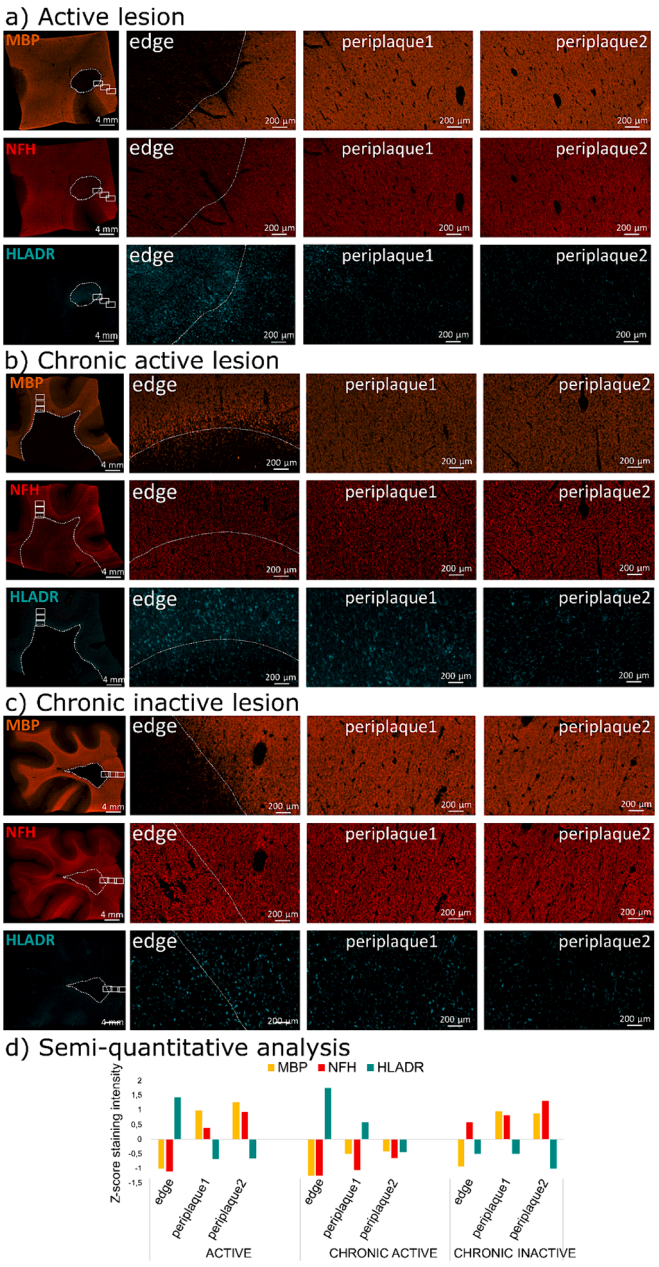

Fig. 4. Histological illustration of the microstructural tissue damage in the core and WM close periplaque (1; 0-2 mm) and distal periplaque (2; 2-4 mm) of (a) an active, (b) a chronic active and, (c) a chronic inactive MS lesion. The white dotted line denotes the edge of the lesion. The first row shows immunofluorescent staining of the myelin basic protein (MBP), found in myelin and oligodendrocytes, the second row shows immunofluorescent staining of neurofilament heavy chain (NFH), a marker for axonal integrity, whereas the third row shows immunofluorescent staining of human leukocyte antigen–DR isotope (HLADR), a marker of antigen presenting myeloid cells (activated microglia/macrophages). A semi-quantitative analysis, based on a z-score normalized intensity of the region observed compared to the whole tissue intensity, is shown in d. See the text for the histopathological description.

lesions. Our model-free approach revealed the superiority of multi-shell over single-shell diffusion MRI, while highlighting the significance of *b*-value selection in diffusion MRI scheme, as different *b*-values exhibit varying sensitivity to brain microstructure. While high *b*-values (e.g. b=5000 s/mm^2) are particularly valuable for describing MS lesions, it is important to note that achieving such high *b*-values may be limited by hardware constraints, including gradient coil capabilities, scanner performance, and signal-to-noise ratio considerations, limiting the generalizability of this method in a clinical setting. Finally, NODDI model demonstrated the best performance, highlighting the ability of advanced multi-shell diffusion models to depict the unique microstructural pattern of CEL, and the severe tissue damage present in PRL+ core and periplaque areas.

4.1. Comparison of diffusion models

NODDI's performance is linked to its interpretable parameters, most notably ecvf (see supplementary analysis in Table S3). This parameter characterizes the extra-neuronal space (Zhang et al., 2012), a specific feature not found in the other diffusion models and deemed relevant to depict the neuropathology of MS lesions. In this study, this parameter is interpreted as cellular tissue infiltration. However, it should be noted that this parameter lacks histopathological validation, and it could also be interpreted as the result of a shift in extracellular diffusivity (Lampinen et al., 2017).

When comparing the performance of the different diffusion models, following NODDI, both MF and DIAMOND exhibited comparable performance, each presenting distinct strengths and weaknesses. MF demonstrated a higher mean auc and better peak performance, while DIAMOND showed greater stability with lower variance and a superior mean rank. However, DIAMOND mainly provides diffusion metrics corresponding to a representation of the multi-shell diffusion signals, with only a marginal gain (auc=0.7302 vs. 0.7292) when compared to the model-free average multi-shell diffusion signals for the differentiation of PRL+ from PRL-. In contrast, MF features biophysically interpretable parameters, offering more informative insights (auc=0.7786) for characterizing the microstructure of MS lesions core.

When comparing the parameters for free water content derived from NODDI (fiso), MF (fcsf$_{MF}$), and DIAMOND (fcsf$_{DMD}$), significant disparities become apparent, particularly between MF and the other two models. Notably, fiso and fcsf$_{DMD}$ exhibit a similar trend across ROI, which differs from the behavior observed with fcsf$_{MF}$. This discrepancy arises from the fact that both NODDI and DIAMOND are analytical diffusion models, describing the free water compartment as a Gaussian isotropic diffusion with a fixed diffusion coefficient of 3.10^{-3} mm^2/s. This representation appears suboptimal, given that the results for fiso and fcsf$_{DMD}$ suggest a decreased water content in CEL (vs other lesion types), a trend inconsistent with physiological expectations (Campbell et al., 2012). Additionally, fiso and fcsf$_{DMD}$ display a somewhat erratic distribution of free water content throughout the NAWM of HC (see Figure S2 (a) and (b) in the supplementary materials). In contrast, fcsf$_{MF}$ from MF reveals a trend more consistent with physiological expectations. It shows a tendency towards increased water content in CEL (albeit not statistically significant) and indicates reduced water content in the NAWM of HC, as illustrated in Figure S2 (c) in the supplementary materials. In order to characterize MS brain pathology, the numerical representation of free water diffusion appears to be a more suitable choice.

In contrast, DTI performance not only fell behind the other diffusion models, but also underperformed compared to the use of T1map, a technique characterized by shorter acquisition and processing times. For the differentiation of PRL+ from PRL-, DTI underperformed as well against the model-free average multi-shell diffusion signals (auc=0.6842 vs. 0.7292), and was marginally better than the model-free average single-shell (b=1000 s/mm^2) diffusion signal (auc=0.6842). The primary limitations of DTI stem from its model assumptions, its inability to represent multi-shell diffusion signals with high *b*-values, and the biologically uninterpretable nature of its metrics (Novikov et al., 2018). These constraints restrict its capability to capture the intricacies of MS lesion microstructural damage. Our findings align with previous studies, reporting a drop in DTI-biology correlation in the context of brain neuroinflammation (Winklewski et al., 2018). Nevertheless, compared to T1map, DTI still offers the possibility to perform additional

analyses such as MRI tractography.

Given the heterogeneous and subtle microstructural changes characterizing MS lesional and extra-lesional brain pathology, our results suggest adopting a combination of diffusion models with interpretable parameters, such as NODDI and MF.

4.2. Pathological interpretation of diffusion analysis

In agreement with our histopathological results, the diffusion analysis revealed extensive demyelination, edema and extra-neuronal cell infiltration in the core of acute lesions and extensive microstructural damage in the periplaque of chronic active lesions (when compared to the surrounding NAWM), extending previous evidence on chronic active lesions microstructure (Hu et al., 2022; Krajnc et al., 2023; Rahmanzadeh et al., 2021) and confirming their destructive phenotype. Combining the parameters of the different diffusion models (based on their respective performance discussed above), we provide a comprehensive qualitative pathological interpretation of our diffusion analysis, portraying acute, chronic active and chronic inactive lesions microstructure relative to NAWM based on four main compartments: axonal (derived from icvf), myelin (derived from RD_{DMD}), free water (derived from $fcsf_{MF}$) and extra-neuronal cell (derived from ecvf) fraction (Fig. 5). These parameters have been adjusted to provide a visually interpretable overview, rather than pure quantitative results. Overall, the diffusion analysis accurately depicts the evolution of a lesion from an acute to a chronic inactive stage, exhibiting reduced edema, similar moderate axonal damage, remyelination (with similar level of myelination in *peri*-PRL- than NAWM) and reduced concentration of extra-neuronal cells. Instead, when evolving into a chronic active stage, our diffusion data suggest ongoing axonal damage, demyelination, and increase of extra-neuronal cells both in the lesion core and periplaque. This microstructural pattern observed in the core and periplaque of PRL+ suggests, consistent with prior studies (Maggi et al., 2021) (Absinta et al., 2019; Maggi et al., 2020), that chronic active inflammation is a major driver of neuroaxonal damage in MS. While this qualitative illustration captures the key features of MS lesion composition, it also emphasizes the limitation of non-interpretable diffusion metrics such as RD to correlate with actual biological compartment, especially in neuroinflammation (Winklewski et al., 2018).

5. Limitations

A substantial limitation in our study was CEL sample size, consisting of only 38 lesions, in contrast to the larger pools of 317 PRL+ and 232 PRL- lesions. This significant discrepancy in sample size severely impacted the statistical power to discern meaningful differences between CEL and other types of chronic MS lesions. However, due to the transient nature of acute inflammation which typically occurs over a brief timeframe of around 4–8 weeks, the frequency of CEL on routine MRI sessions is relatively low. Additionally, the small size and the incomplete MRI protocol adopted for the HC cohort may have influenced the MS-HC NAWM comparison presented here. Finally, our study

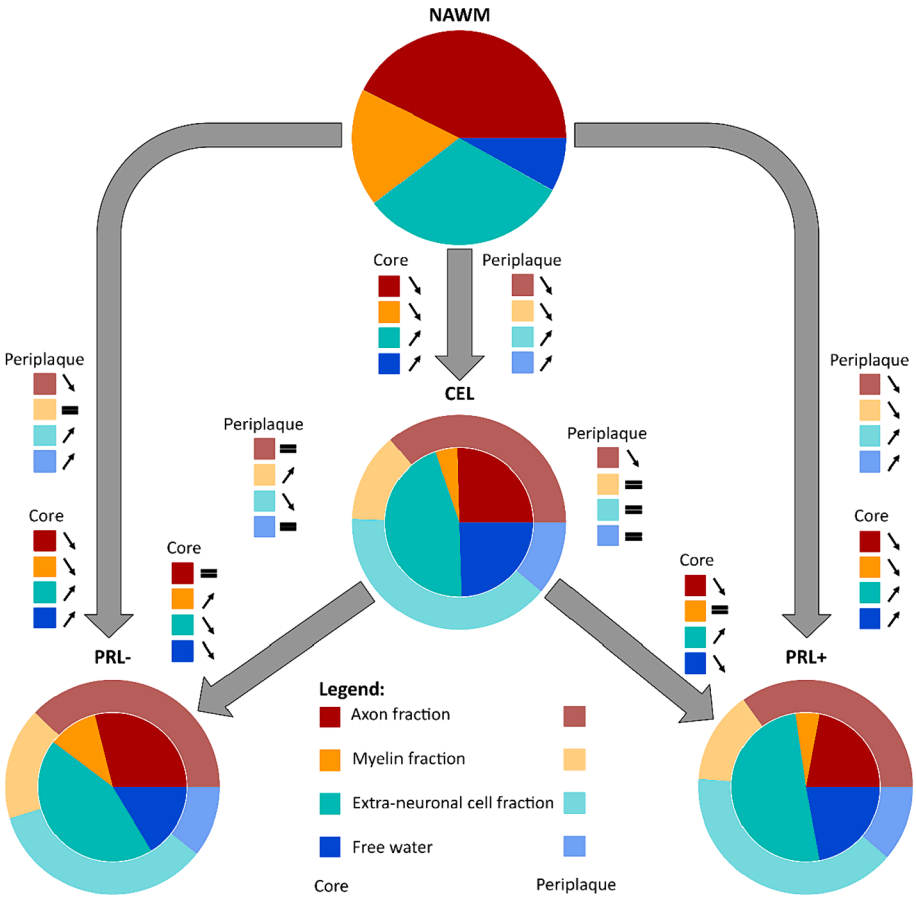

Fig. 5. Graphical representation of the evolution of active lesions (CEL) into chronic inactive lesions (PRL-) or chronic active lesions (PRL+), relative to the normal-appearing white matter (NAWM), based on 4 pathologically relevant microstructural compartments: axonal (derived from icvf; red), myelin (derived from RD_{DMD}; orange), free water (derived from $fcsf_{MF}$; blue) and extra-neuronal cell (derived from ecvf; turquoise) fraction. Active lesions are characterized by the presence of edema and pronounced cellular infiltration, with moderate axonal damage and high demyelination. When evolving into a chronic inactive stage, inflammation tends to resolve (less cellular infiltration and edema), potentially contributing to remyelination. On the other hand, when CEL evolve into chronic active lesions, both axonal and myelin damage are prominent, while the edema resorbs itself and the fraction of extra-neuronal cells increases.

encountered limitations stemming from the relatively poor resolution of diffusion MRI. This limited resolution hindered our ability to investigate the immediate periplaque area, especially at the lesion edges, and potentially introduced a bias due to partial volume effect in the analysis of smaller ROI, corresponding to few voxels on the diffusion images. These small voxel populations were susceptible to noise in both acquisition and processing, potentially affecting the accuracy of our results. To mitigate this bias, lesions included in the analysis had a minimum size of 24 mm^3.

6. Conclusion

In conclusion, multi-shell diffusion MRI can accurately characterize the heterogeneous architecture of MS lesional and extra-lesional pathology, further extending the potential of this technique to detect microstructural alterations *in vivo*. Although the qualitative lesion microstructural model presented here recapitulates the key features of MS lesion pathology (Fig. 5), it also emphasizes the limitation of non-interpretable representative diffusion metrics to correlate with actual biological compartments, especially in neuroinflammation. We believe that the choice of multi-shell diffusion MRI schemes and appropriate diffusion models is paramount for achieving precise microstructural estimation of subtle and specific damage patterns. In order to achieve accurate results in the context of MS, we recommend the use of multi-compartment diffusion models based on biophysically interpretable metrics.

Funding

Colin Vanden Bulcke has the financial support of the Fonds de Recherche Clinique (FRC), Université catholique de Louvain.

Anna Stölting has the financial support of the Fédération Wallonie Bruxelles - Fonds Spéciaux de Recherche (F.S.R.), Université catholique de Louvain.

Dragan Maric and Benoît Macq have nothing to disclose.

Martina Absinta received research support from the Conrad N. Hilton Foundation (Marilyn Hilton Bridging Award for Physician-Scientists, grant #17313), the Roche Foundation for Independent Research, the Cariplo Foundation (grant #1677), the FRRB Early Career Award (grant #1750327), the National MS Society (NMSS-RFA 2203-39325) and the International Progressive MS alliance (PA-2107-38081). She received consultancy and/or speaker honoraria from Biogen, GSK, Sanofi, Abata Therapeutics, Viatris, and Immunic Therapeutics.

Pietro Maggi is supported by the Fonds de Recherche Clinique (FRC), Université catholique de Louvain, by the Fund for Scientific Research (F.R.S.–FNRS, grant #40008331), and by the Fondation Charcot Stichting Research Fund 2023.

CRediT authorship contribution statement

Colin Vanden Bulcke: Writing – review & editing, Writing – original draft, Visualization, Validation, Methodology, Investigation, Formal analysis, Data curation, Conceptualization. **Anna Stölting:** Writing – review & editing, Writing – original draft, Formal analysis, Data curation. **Dragan Maric:** Writing – review & editing, Writing – original draft, Data curation. **Benoît Macq:** Writing – review & editing, Writing – original draft, Supervision. **Martina Absinta:** Writing – review & editing, Writing – original draft, Data curation. **Pietro Maggi:** Writing – review & editing, Writing – original draft, Supervision, Investigation, Conceptualization.

Declaration of Competing Interest

The authors declare that they have no known competing financial interests or personal relationships that could have appeared to influence the work reported in this paper.

Data availability

The authors do not have permission to share data.

Acknowledgements

The authors thank the study participants; the neuroimmunology clinic of Cliniques Universitaires Saint-Luc for recruiting and evaluating the participants and for coordinating the scans; Stefan Skare (Karolinska University Hospital), Thierry Duprez, Sébastien de Laever (Cliniques universitaires Saint-Luc), Laurence Dricot (Université catholique de Louvain) and Julie Poujol (GE Healthcare) for assistance with 3T MRI scan acquisition and analysis; the Netherlands Brain Bank (NBB; https://www.brainbank.nl/) for providing the autopsy MS brain tissue; Daniel S. Reich (NINDS, NIH, USA) for help with the multiplex immunostainings; Céline Bugli for help with statistical analyses.

Appendix A. Supplementary data

Supplementary data to this article can be found online at https://doi.org/10.1016/j.nicl.2024.103593.

References

Absinta, M., Sati, P., Gaitán, M.I., Maggi, P., Cortese, I.C.M., Filippi, M., Reich, D.S., 2013. Seven-tesla phase imaging of acute multiple sclerosis lesions: a new window into the inflammatory process. Ann. Neurol. 74 (5), 669–678. https://doi.org/10.1002/ana.23959.

Absinta, M., Sati, P., Schindler, M., Leibovitch, E.C., Ohayon, J., Wu, T., Meani, A., Filippi, M., Jacobson, S., Cortese, I.C.M., Reich, D.S., 2016. Persistent 7-tesla phase rim predicts poor outcome in new multiple sclerosis patient lesions. J. Clin. Invest. 126 (7), 2597–2609. https://doi.org/10.1172/JCI86198.

Absinta, M., Sati, P., Masuzzo, F., Nair, G., Sethi, V., Kolb, H., Ohayon, J., Wu, T., Cortese, I.C.M., Reich, D.S., 2019. Association of Chronic Active Multiple Sclerosis Lesions with Disability in Vivo. JAMA Neurol. 76 (12), 1474–1483. https://doi.org/10.1001/jamaneurol.2019.2399.

Absinta, M., Maric, D., Gharagozloo, M., Garton, T., Smith, M.D., Jin, J., Fitzgerald, K.C., Song, A., Liu, P., Lin, J.-P., Wu, T., Johnson, K.R., McGavern, D.B., Schafer, D.P., Calabresi, P.A., Reich, D.S., 2021. A lymphocyte–microglia–astrocyte axis in chronic active multiple sclerosis. Article 7878 Nature 597 (7878). https://doi.org/10.1038/s41586-021-03892-7.

Alexander, A.L., Lee, J.E., Lazar, M., Field, A.S., 2007. Diffusion tensor imaging of the brain. Neurotherapeutics 4 (3), 316–329. https://doi.org/10.1016/j.nurt.2007.05.011.

Andersson, J.L.R., Skare, S., Ashburner, J., 2003. How to correct susceptibility distortions in spin-echo echo-planar images: application to diffusion tensor imaging. Neuroimage 20 (2), 870–888. https://doi.org/10.1016/S1053-8119(03)00336-7.

Andersson, J.L.R., Sotiropoulos, S.N., 2016. An integrated approach to correction for off-resonance effects and subject movement in diffusion MR imaging. Neuroimage 125, 1063–1078. https://doi.org/10.1016/j.neuroimage.2015.10.019.

Avants, B., Tustison, N., Song, G., 2008. Advanced normalization tools (ANTS). Insight J. 1–35 https://doi.org/10.54294/uvnhin.

Bagnato, F., Sati, P., Hemond, C. C., Elliott, C., Gauthier, S. A., Harrison, D. M., Mainero, C., Oh, J., Pitt, D., Shinohara, R. T., Smith, S. A., Trapp, B., Azevedo, C. J., Calabresi, P. A., Henry, R. G., Laule, C., Ontaneda, D., Rooney, W. D., Sicotte, N. L., … on behalf of the NAIMS Cooperative. (2024). Imaging chronic active lesions in multiple sclerosis: A consensus statement. *Brain*, awae013. DOI: 10.1093/brain/awae013.

Campbell, Z., Sahm, D., Donohue, K., Jamison, J., Davis, M., Pellicano, C., Auh, S., Ohayon, J., Frank, J.A., Richert, N., Bagnato, F., 2012. Characterizing contrast-enhancing and re-enhancing lesions in multiple sclerosis. Neurology 78 (19), 1493–1499. https://doi.org/10.1212/WNL.0b013e3182553bd2.

Cerri, S., Puonti, O., Meier, D.S., Wuerfel, J., Mühlau, M., Siebner, H.R., Van Leemput, K., 2021. A contrast-adaptive method for simultaneous whole-brain and lesion segmentation in multiple sclerosis. Neuroimage 225. https://doi.org/10.1016/j.neuroimage.2020.117471.

Dal-Bianco, A., Grabner, G., Kronnerwetter, C., Weber, M., Kornek, B., Kasprian, G., Berger, T., Leutmezer, F., Rommer, P.S., Trattnig, S., Lassmann, H., Hametner, S., 2021. Long-term evolution of multiple sclerosis iron rim lesions in 7 T MRI. Brain 144 (3), 833–847. https://doi.org/10.1093/brain/awaa436.

Fischl, B., Salat, D.H., Busa, E., Albert, M., Dieterich, M., Haselgrove, C., van der Kouwe, A., Killiany, R., Kennedy, D., Klaveness, S., Montillo, A., Makris, N., Rosen, B., Dale, A.M., 2002. Whole brain segmentation: automated labeling of neuroanatomical structures in the human brain. Neuron 33 (3), 341–355. https://doi.org/10.1016/S0896-6273(02)00569-X.

Hemond, C.C., Baek, J., Ionete, C., Reich, D.S., 2022. Paramagnetic rim lesions are associated with pathogenic CSF profiles and worse clinical status in multiple sclerosis: a retrospective cross-sectional study. Multiple Sclerosis (houndmills, Basingstoke, England) 28 (13), 2046–2056. https://doi.org/10.1177/13524585221102921.

Hori, M., Maekawa, T., Kamiya, K., Hagiwara, A., Goto, M., Takemura, M.Y., Fujita, S., Andica, C., Kamagata, K., Cohen-Adad, J., Aoki, S., 2022. Advanced diffusion MR imaging for multiple sclerosis in the brain and spinal cord. Magn. Reson. Med. Sci. 21 (1), 58–70. https://doi.org/10.2463/mrms.rev.2021-0091.

Hu, H., Ye, L., Ding, S., Zhu, Q., Yan, Z., Chen, X., Chen, G., Feng, X., Li, Q., Li, Y., 2022. The heterogeneity of tissue destruction between iron rim lesions and non-iron rim lesions in multiple sclerosis: a diffusion MRI study. Mult. Scler. Relat. Disord. 66 https://doi.org/10.1016/j.msard.2022.104070.

Jenkinson, M., Pechaud, M., & Smith, S. (2005). BET2: MR-Based Estimation of Brain, Skull and Scalp Surfaces. Eleventh Annual Meeting of the Organization for Human Brain Mapping, 2005. https://cir.nii.ac.jp/crid/1573950400559824000.

Kolb, H., Absinta, M., Beck, E.S., Ha, S.-K., Song, Y., Norato, G., Cortese, I., Sati, P., Nair, G., Reich, D.S., 2021. 7T MRI differentiates remyelinated from demyelinated multiple sclerosis lesions. Ann. Neurol. 90 (4), 612–626. https://doi.org/10.1002/ana.26194.

Krajnc, N., Schmidbauer, V., Leinkauf, J., Haider, L., Bsteh, G., Kasprian, G., Leutmezer, F., Kornek, B., Rommer, P.S., Berger, T., Lassmann, H., Dal-Bianco, A., Hametner, S., 2023. Paramagnetic rim lesions lead to pronounced diffuse periplaque white matter damage in multiple sclerosis, 13524585231197954 Mult. Scler. J.. https://doi.org/10.1177/13524585231197954.

Kutzelnigg, A., Lucchinetti, C.F., Stadelmann, C., Brück, W., Helmut, R., Bergmann, M., Schmidbauer, M., Parisi, J.E., Lassmann, H., 2005. Cortical demyelination and diffuse white matter injury in multiple sclerosis. Brain J. Neurol. 128 (Pt 11) https://doi.org/10.1093/brain/awh641.

Lampinen, B., Szczepankiewicz, F., Mårtensson, J., van Westen, D., Sundgren, P.C., Nilsson, M., 2017. Neurite density imaging versus imaging of microscopic anisotropy in diffusion MRI: a model comparison using spherical tensor encoding. Neuroimage 147, 517–531. https://doi.org/10.1016/j.neuroimage.2016.11.053.

Lucchinetti, C., Brück, W., Parisi, J., Scheithauer, B., Rodriguez, M., Lassmann, H., 2000. Heterogeneity of multiple sclerosis lesions: implications for the pathogenesis of demyelination. Ann. Neurol. 47 (6), 707–717.

Maggi, P., Vanden Bulcke, C., Pedrini, E., Bugli, C., Sellimi, A., Wynen, M., Stölting, A., Mullins, W. A., Kalaitzidis, G., Lolli, V., Perrotta, G., El Sankari, S., Duprez, T., Li, X., Calabresi, P. A., van Pesch, V., Reich, D., & Absinta, M. (2023). B-Cell Depletion Therapy Does Not Resolve Chronic Active Multiple Sclerosis Lesions. *eBiomedecine, in press*.

Maggi, P., Sati, P., Nair, G., Cortese, I.C.M., Jacobson, S., Smith, B.R., Nath, A., Ohayon, J., van Pesch, V., Perrotta, G., Pot, C., Théaudin, M., Martinelli, V., Scotti, R., Wu, T., Du Pasquier, R., Calabresi, P.A., Filippi, M., Reich, D.S., Absinta, M., 2020. Paramagnetic rim lesions are specific to multiple sclerosis: an international multicenter 3T MRI study. Ann. Neurol. 88 (5), 1034–1042. https://doi.org/10.1002/ana.25877.

Maggi, P., Kuhle, J., Schädelin, S., van der Meer, F., Weigel, M., Galbusera, R., Mathias, A., Lu, P.-J., Rahmanzadeh, R., Benkert, P., La Rosa, F., Bach Cuadra, M., Sati, P., Théaudin, M., Pot, C., van Pesch, V., Leppert, D., Stadelmann, C., Kappos, L., Granziera, C., 2021. Chronic white matter inflammation and serum neurofilament levels in multiple sclerosis. Neurology 97 (6), e543–e553. https://doi.org/10.1212/WNL.0000000000012326.

Mustafi, S.M., Harezlak, J., Kodiweera, C., Randolph, J.S., Ford, J.C., Wishart, H.A., Wu, Y.-C., 2019. Detecting white matter alterations in multiple sclerosis using advanced diffusion magnetic resonance imaging. Neural Regen. Res. 14 (1), 114–123. https://doi.org/10.4103/1673-5374.243716.

Novikov, D.S., Kiselev, V.G., Jespersen, S.N., 2018. On modeling. Magn. Reson. Med. 79 (6), 3172–3193. https://doi.org/10.1002/mrm.27101.

Otsu, N., 1979. A threshold selection method from gray-level histograms. IEEE Trans. Syst. Man Cybern. 9 (1), 62–66. https://doi.org/10.1109/TSMC.1979.4310076.

Rahmanzadeh, R., Lu, P.-J., Barakovic, M., Weigel, M., Maggi, P., Nguyen, T.D., Schiavi, S., Daducci, A., La Rosa, F., Schaedelin, S., Absinta, M., Reich, D.S., Sati, P., Wang, Y., Bach Cuadra, M., Radue, E.W., Kuhle, J., Kappos, L., Granziera, C., 2021. Myelin and axon pathology in multiple sclerosis assessed by myelin water and multi-shell diffusion imaging. Brain: A J. Neurol. 144 (6), 1684–1696. https://doi.org/10.1093/brain/awab088.

Reich, D.S., Lucchinetti, C.F., Calabresi, P.A., 2018. Multiple sclerosis. N. Engl. J. Med. 378 (2), 169–180. https://doi.org/10.1056/NEJMra1401483.

Rensonnet, G., Scherrer, B., Girard, G., Jankovski, A., Warfield, S.K., Macq, B., Thiran, J.-P., Taquet, M., 2019. Towards microstructure fingerprinting: estimation of tissue properties from a dictionary of Monte Carlo diffusion MRI simulations. Neuroimage 184, 964–980. https://doi.org/10.1016/j.neuroimage.2018.09.076.

Sati, P., Thomasson, D.M., Li, N., Pham, D.L., Biassou, N.M., Reich, D.S., Butman, J.A., 2014. Rapid, high-resolution, whole-brain, susceptibility-based MRI of multiple sclerosis. Multiple Sclerosis (houndmills, Basingstoke, England) 20 (11), 1464–1470. https://doi.org/10.1177/1352458514525868.

Scherrer, B., Schwartzman, A., Taquet, M., Sahin, M., Prabhu, S.P., Warfield, S.K., 2016. Characterizing brain tissue by assessment of the distribution of anisotropic microstructural environments in diffusion-compartment imaging (DIAMOND). Magn. Reson. Med. 76 (3), 963–977. https://doi.org/10.1002/mrm.25912.

Thompson, A.J., Banwell, B.L., Barkhof, F., Carroll, W.M., Coetzee, T., Comi, G., Correale, J., Fazekas, F., Filippi, M., Freedman, M.S., Fujihara, K., Galetta, S.L., Hartung, H.P., Kappos, L., Lublin, F.D., Marrie, R.A., Miller, A.E., Miller, D.H., Montalban, X., Cohen, J.A., 2018. Diagnosis of multiple sclerosis: 2017 revisions of the McDonald criteria. The Lancet Neurology 17 (2), 162–173. https://doi.org/10.1016/S1474-4422(17)30470-2.

Vanden Bulcke, C., Wynen, M., Detobel, J., La Rosa, F., Absinta, M., Dricot, L., Macq, B., Bach Cuadra, M., Maggi, P., 2022. BMAT: an open-source BIDS managing and analysis tool. NeuroImage: Clinical 36. https://doi.org/10.1016/j.nicl.2022.103252.

Veraart, J., Sijbers, J., Sunaert, S., Leemans, A., Jeurissen, B., 2013. Weighted linear least squares estimation of diffusion MRI parameters: strengths, limitations, and pitfalls. Neuroimage 81, 335–346. https://doi.org/10.1016/j.neuroimage.2013.05.028.

Veraart, J., Novikov, D.S., Christiaens, D., Ades-Aron, B., Sijbers, J., Fieremans, E., 2016. Denoising of diffusion MRI using random matrix theory. Neuroimage 142, 394–406. https://doi.org/10.1016/j.neuroimage.2016.08.016.

Winklewski, P.J., Sabisz, A., Naumczyk, P., Jodzio, K., Szurowska, E., Szarmach, A., 2018. Understanding the physiopathology behind axial and radial diffusivity changes—What do we know? Front. Neurol. 9, 92. https://doi.org/10.3389/fneur.2018.00092.

Zhang, H., Schneider, T., Wheeler-Kingshott, C.A., Alexander, D.C., 2012. NODDI: practical in vivo neurite orientation dispersion and density imaging of the human brain. Neuroimage 61 (4), 1000–1016. https://doi.org/10.1016/j.neuroimage.2012.03.072.